Supporting Information

Synergistic Regulation of Conductance via Functional Groups and Connection Topology in Cyclopentadienone Molecular Junctions

Zhe-Hao Bai,†[a] Xin Zuo,†[b] Ming-Hao Wu,[a] Ye-Hao Ding,[a] Wen-Rui Xu,[a] Yan-Hou Geng,[c,d] Jian-Feng Yan,*[,a] Li-Chuan Chen,*[,b] Dong Xiang*[,b] and Yao-Feng Yuan*[,a]

([a] *Key Laboratory of Molecule Synthesis and Function Discovery, Fujian Province University, College of Chemistry at Fuzhou University, Fuzhou, Fujian, 350108, China*)
([b] *Institute of Modern Optics, College of Electronic Information and Optical Engineering, Nankai University, Tianjin 300350, China*)
([c] *Joint School of National University of Singapore and Tianjin University, International Campus of Tianjin University, Fuzhou 350207, China*)
([d] *School of Materials Science and Engineering and Tianjin Key Laboratory of Molecular Optoelectronic Science, Tianjin University, Tianjin 300072, China*)
Email: yanjianfeng@fzu.edu.cn; chen.lichuan@nankai.edu.cn; xiangdongde@nankai.edu.cn; yaofeng_yuan@fzu.edu.cn

Table of Contents

1. Synthetic procedures

1.1 Synthesis of 3,4-bis[4-(methylsulfanyl)phenyl]-2,5-diphenylcyclopenta-2,4-dien-1-one (***o*-CO**)

In a 100 mL three-neck flask fitted with a magnetic stir bar, the vessel was handled using standard Schlenk techniques. Then 1,2-bis[4-(methylsulfanyl)phenyl]ethane-1,2-dione (302.0 mg, 1.00 mmol), 1,3-diphenylpropan-2-one (210.0 mg, 1.00 mmol), and KOH (16.8 mg, 0.30 mmol) were added sequentially. After that, anhydrous ethanol (20 mL) was added. The mixture was stirred at room temperature for 0.5 h. Progress was monitored by TLC (PE/DCM = 5/1, v/v), R_f = 0.34. Upon completion, the mixture was cooled in an ice bath. The precipitated solid was collected by vacuum filtration and washed with ethanol (15 mL). The crude product was purified by recrystallization from *n*-heptane to give ***o*-CO** as a black-purple solid (259.7 mg, 0.55 mmol, 55% yield). m.p. 184–186 °C. ^{1}H NMR (500 MHz, $CDCl_3$) δ 7.24 (q, *J* = 7.2 Hz, 10H, phenyl-H), 7.03 (d, *J* = 8.4 Hz, 4H, phenyl-H), 6.84 (d, *J* = 8.4 Hz, 4H, phenyl-H), 2.46 (s, 6H, -SMe). ^{13}C NMR (126 MHz, $CDCl_3$) δ 200.2, 153.7, 139.9, 131.0, 130.3, 130.1, 129.3, 128.2, 127.6, 125.5, 125.2, 15.1. HRMS (ESI$^+$) m/z calcd for $C_{31}H_{24}S_2O$: 476.1263 $[M]^+$; found 476.1271.

1.2 Synthesis of 1,3-bis[4-(methylsulfanyl)phenyl]-4,5-diphenylcyclopenta-1,3-diene (***o*-CH$_2$**)

In a 100 mL three-neck round-bottom flask equipped with a magnetic stir bar, the vessel was handled using standard Schlenk techniques. Anhydrous diethyl ether (30 mL) and ***o*-CO** (1000.0 mg, 2.10 mmol) were added. The suspension was cooled in an ice bath. $AlCl_3$ (570.0 mg, 4.27 mmol) was added, followed by slow addition of $LiAlH_4$ (160.0 mg, 4.22 mmol). During this process, the mixture color changed from black-purple to yellow-green. The reaction mixture was then stirred under reflux for 24 h. Progress was monitored by TLC (PE/DCM = 2/1, v/v), R_f = 0.28. After cooling to room temperature, excess $LiAlH_4$ was carefully quenched with dilute HCl (8 mL). The ether layer was separated, and the aqueous phase was extracted with DCM (3 × 10 mL) until no further residue was observed. The combined organic layers were washed with saturated $NaHCO_3$ solution (3 × 10 mL), and the solvent was removed under reduced pressure to afford the crude product. Purification by column chromatography (PE/DCM = 3/1, v/v) afforded the yellow fraction. After rotary evaporation and recrystallization from *n*-

heptane, ***o*-CH₂** was obtained as a pale yellow solid (460.0 mg, 1.00 mmol, 47% yield). m.p. 182–183 °C. ^{1}H NMR (500 MHz, $CDCl_3$) δ 7.18 (d, J = 4.3 Hz, 8H, phenyl-H), 7.15–7.11 (m, 2H, phenyl-H), 7.03 (d, J = 8.3 Hz, 4H, phenyl-H), 6.87 (d, J = 8.3 Hz, 4H, phenyl-H), 3.98 (s, 2H, Cp-H), 2.44 (s, 6H, -SMe). ^{13}C NMR (126 MHz, $CDCl_3$) δ 143.7, 140.2, 136.8, 136.6, 133.1, 130.5, 128.3, 128.0, 126.6, 125.9, 46.2, 29.8. HRMS (ESI^+) m/z calcd for $C_{31}H_{26}S_2$+H^+: 463.1549 $[M+H]^+$; found, 463.1543.

1.3 Synthesis of 3,4-bis[4-(methylsulfanyl)phenyl]-2,5-diphenylcyclopenta-2,4-dien-1-ol (***o*-CHOH**)

In a 100 mL three-neck round-bottom flask equipped with a magnetic stir bar, the apparatus was handled using standard Schlenk techniques. Methanol (5 mL) and ***o*-CO** (118.0 mg, 0.25 mmol) were added. The mixture was cooled in an ice bath. $NaBH_4$ (9.8 mg, 0.26 mmol) was added in two slow portions. During the addition, the color changed from black-purple to yellow. The mixture was then stirred at ambient temperature for 2 h. Progress was monitored by TLC (PE/DCM = 1/1, v/v), R_f = 0.52. After completion, the reaction mixture was poured into 20 mL of 1 mol·L^{-1} aqueous NaOH solution and cooled thoroughly in an ice bath. The resulting solid was collected by vacuum filtration and washed with methanol (15 mL). The crude product was recrystallized from *n*-heptane to give ***o*-CHOH** as a yellow solid (43.4 mg, 0.09 mmol, 37% yield). m.p. 213–216 °C. ^{1}H NMR (500 MHz, $CDCl_3$) δ 7.35 (d, J = 7.2 Hz, 4H, phenyl-H), 7.23 (d, J = 7.6 Hz, 6H, phenyl-H), 7.03 (d, J = 8.3 Hz, 4H, phenyl-H), 6.91 (d, J = 8.3 Hz, 4H, phenyl-H), 5.70 (d, J = 7.2 Hz, 1H, Cp-H), 2.45 (s, 6H, -SMe). ^{13}C NMR (126 MHz, $CDCl_3$) δ 142.2, 142.0, 137.5, 134.5, 131.9, 130.3, 129.0, 128.4, 127.2, 125.8, 80.1, 15.4. HRMS (ESI^+) m/z calcd for $C_{31}H_{26}S_2O$+H^+: 479.1498 $[M+H]^+$; found, 479.1497.

1.4 Synthesis of 2,5-bis[4-(methylsulfanyl)phenyl]-3,4-diphenylcyclopenta-2,4-dien-1-one (***m*-CO**)

The synthesis of ***m*-CO** was performed by the same procedure used for ***o*-CO**: a mixture of 1,3-bis[4-(methylsulfanyl)phenyl]propan-2-one (228.0 mg, 0.75 mmol), 1,2-diphenylethane-1,2-dione (210.0 mg, 1.00 mmol), and KOH (16.8 mg, 0.30 mmol) was employed, furnishing ***m*-CO** as a pure black-purple solid (332.4 mg, 0.70 mmol, 93% yield). m.p. 226–228 °C. ^{1}H NMR (500 MHz, $CDCl_3$) δ 7.25 (t, J = 7.4 Hz, 2H, phenyl-H), 7.18 (t, J = 8.4 Hz, 8H, phenyl-H), 7.11 (d, J = 8.6 Hz, 4H, phenyl-H), 6.93 (d, J = 7.1 Hz, 4H, phenyl-H), 2.45 (s, 6H, -SMe). ^{13}C NMR (126 MHz, $CDCl_3$) δ 200.6, 154.2,

138.2, 133.2, 130.5, 129.4, 128.6, 128.2, 127.4, 125.8, 124.7, 15.47. HRMS (ESI^+) m/z calcd for $C_{31}H_{24}S_2O+H^+$: 477.1341 $[M+H]^+$; found: 477.1329.

1.5 Synthesis of 1,3-bis[4-(methylsulfanyl)phenyl]-4,5-diphenylcyclopenta-1,3-diene (***m*-CH$_2$**)

The synthesis of ***m*-CH$_2$** was carried out following the same protocol as for ***o*-CH$_2$**: ***m*-CO** (1000.0 mg, 2.10 mmol), $AlCl_3$ (570.0 mg, 4.30 mmol), and $LiAlH_4$ (160.0 mg, 4.30 mmol) were combined in anhydrous diethyl ether (30 mL), and the reaction furnished ***m*-CH$_2$** as a pure pale-yellow solid (660.0 mg, 1.43 mmol, 68% yield). m.p. 203–206 °C. ^{1}H NMR (500 MHz, $CDCl_3$) δ 7.21–7.14 (m, 6H, phenyl-H), 7.11 (d, *J* = 8.5 Hz, 4H, phenyl-H), 7.05 (d, *J* = 8.5 Hz, 4H, phenyl-H), 6.98 (dd, *J* = 6.6, 3.0 Hz, 4H, phenyl-H), 3.98 (s, 2H, Cp-H), 2.44 (s, 6H, -SMe). ^{13}C NMR (126 MHz, $CDCl_3$) δ 144.6, 138.9, 136.7, 136.4, 133.3, 129.9, 128.2, 128.2, 126.9, 126.2, 45.5, 15.7. HRMS (ESI^+) m/z calcd for $C_{31}H_{26}S_2$: 462.1470 $[M]^+$; found 462.1465.

1.6 Synthesis of 2,5-bis[4-(methylsulfanyl)phenyl]-3,4-diphenylcyclopenta-2,4-dien-1-ol (***m*-CHOH**)

The synthesis of ***m*-CHOH** was carried out analogously to that of ***o*-CHOH**: a mixture of ***m*-CO** (118.0 mg, 0.25 mmol), $NaBH_4$ (9.8 mg, 0.26 mmol), and MeOH (5 mL) furnished ***m*-CHOH** as a pure yellow solid (62.4 mg, 0.13 mmol, 53% yield). m.p. 214–216 °C. ^{1}H NMR (500 MHz, $CDCl_3$) δ 7.28 (s, 4H, phenyl-H), 7.20–7.14 (m, 6H, phenyl-H), 7.09 (d, *J* = 8.5 Hz, 4H, phenyl-H), 7.00 (dd, *J* = 6.4, 3.0 Hz, 4H, phenyl-H), 5.70 (d, *J* = 7.7 Hz, 1H, Cp-H), 2.44 (s, 6H, -SMe), 1.90 (d, *J* = 7.7 Hz, 1H, -OH). ^{13}C NMR (126 MHz, $CDCl_3$) δ 142.9, 140.9, 137.3, 135.6, 131.1, 129.7, 129.1, 128.3, 127.3, 126.1, 79.7, 15.6. HRMS (ESI^+) m/z calcd for $C_{31}H_{26}S_2O+H^+$: 479.1498 $[M+H]^+$; found, 479.1490.

2. NMR characterization

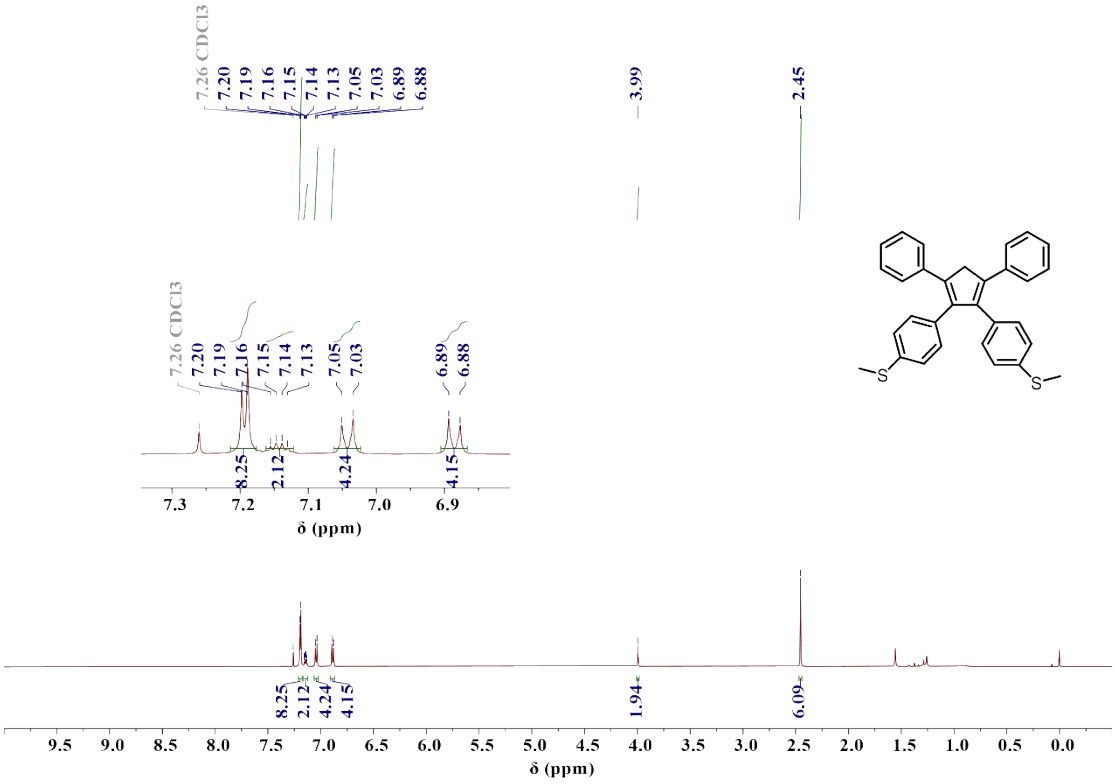

Fig. S1 ^{1}H NMR spectrum of ***o*-CH$_2$** in $CDCl_3$.

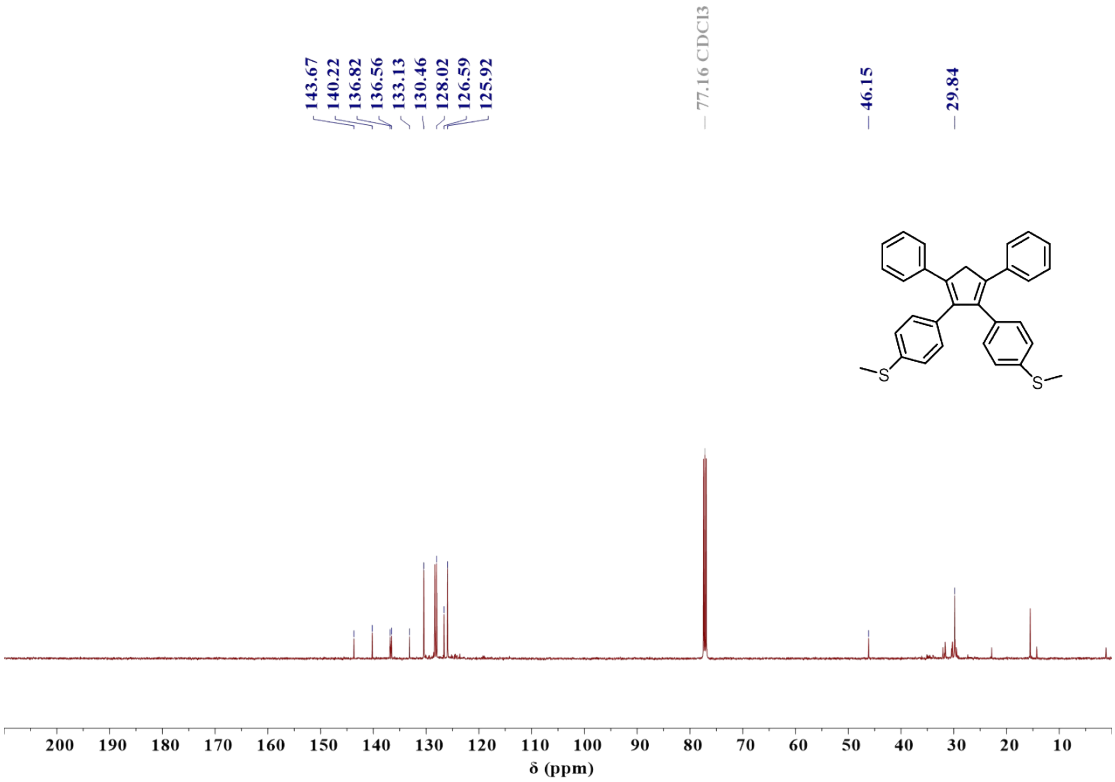

Fig. S2 ^{13}C NMR spectrum of ***o*-CH$_2$** in $CDCl_3$.

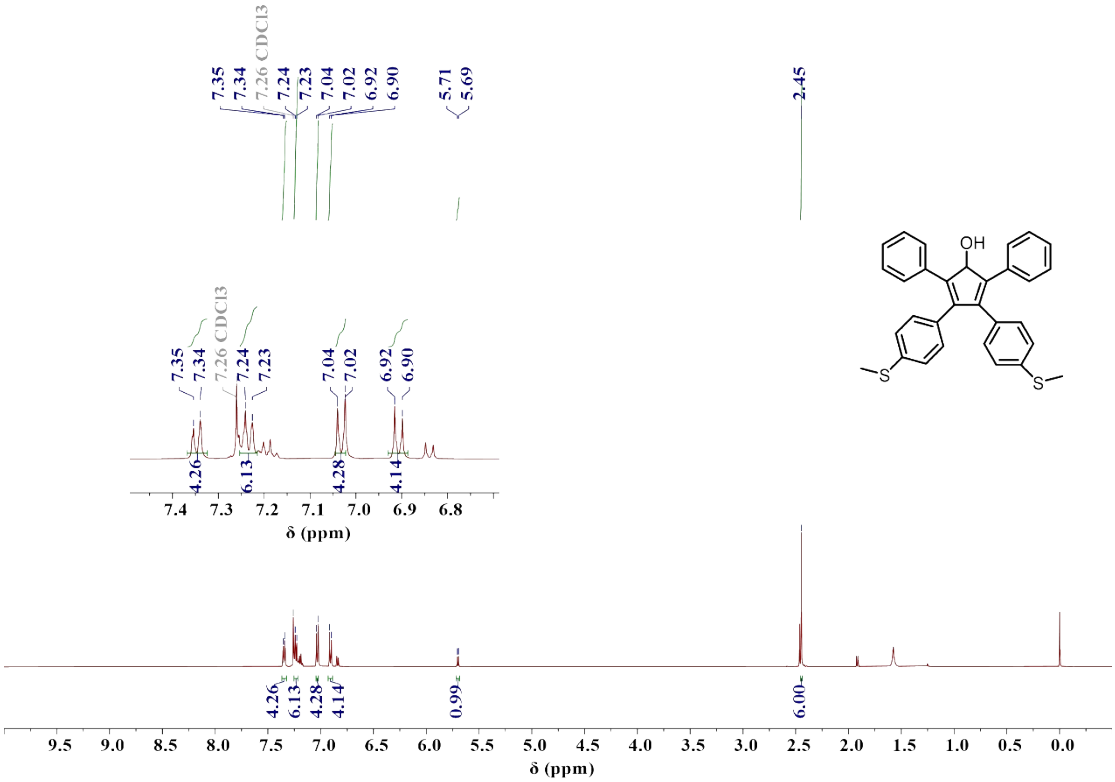

Fig. S3 ^{1}H NMR spectrum of ***o*-CHOH** in $CDCl_3$.

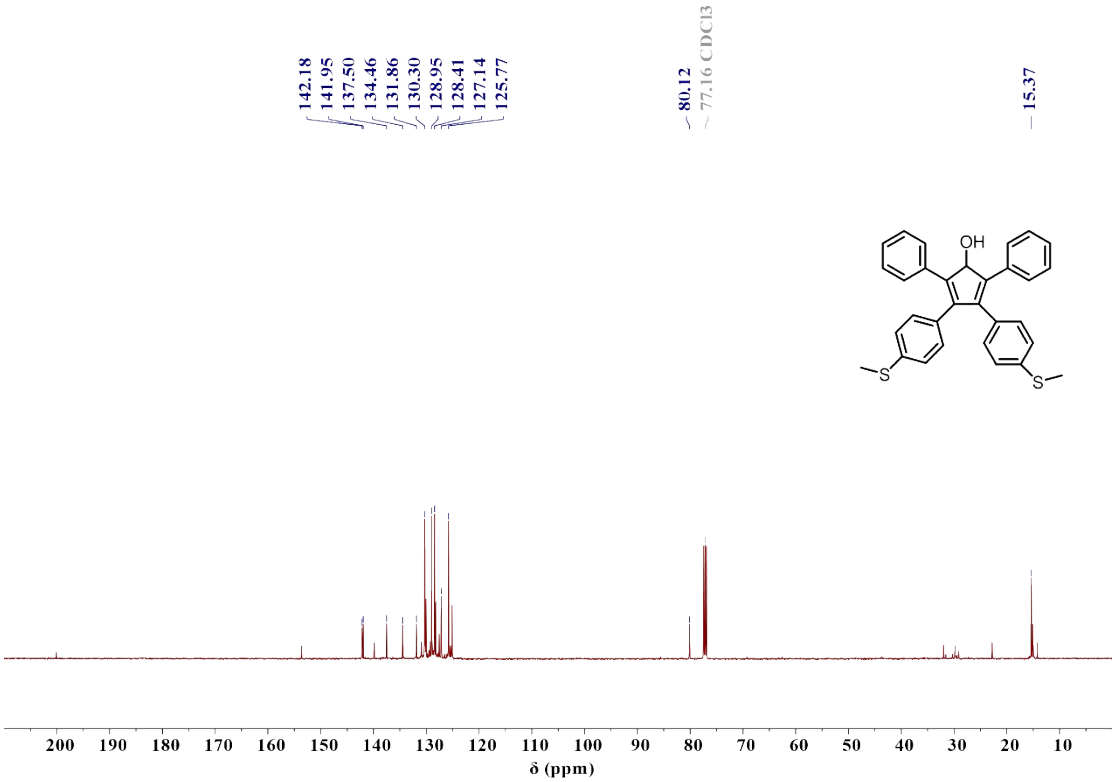

Fig. S4 ^{13}C NMR spectrum of ***o*-CHOH** in $CDCl_3$.

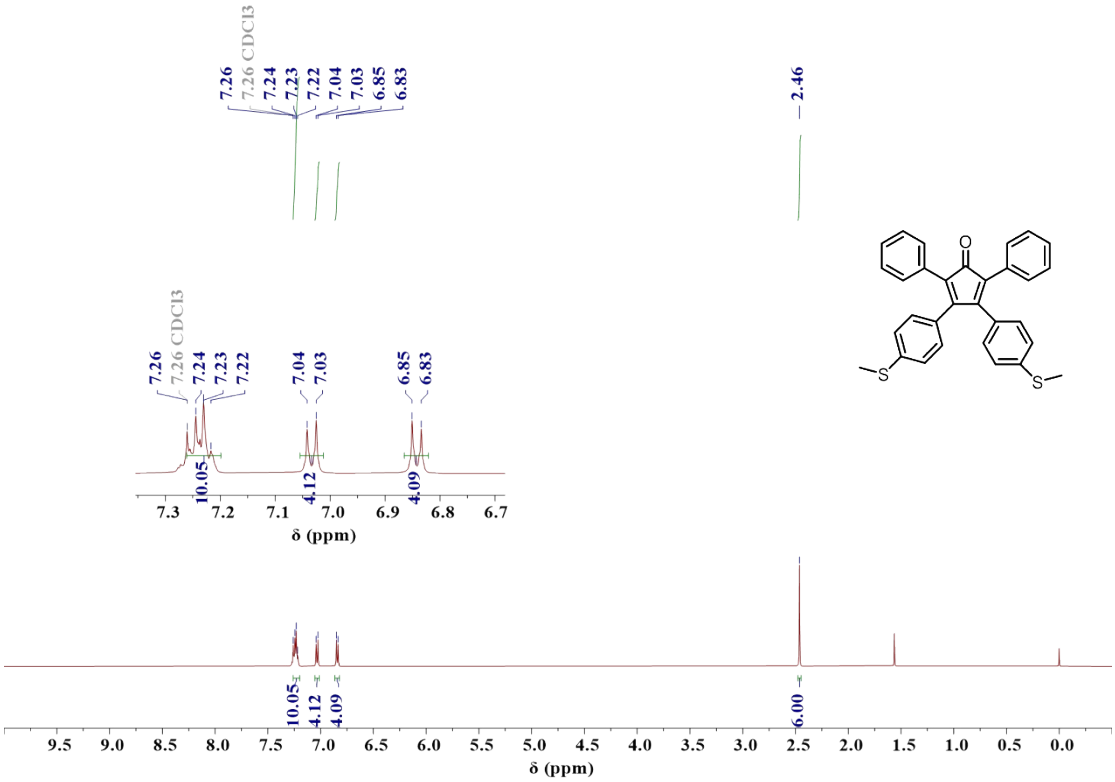

Fig. S5 ^{1}H NMR spectrum of ***o*-CO** in $CDCl_3$.

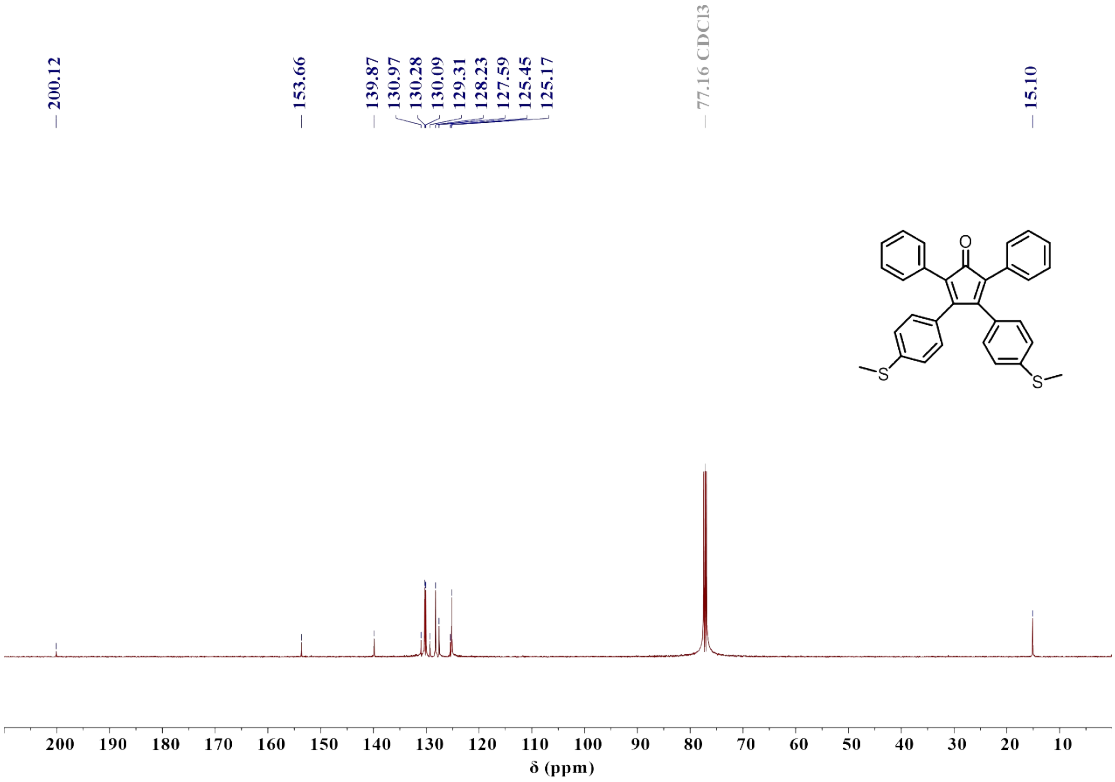

Fig. S6 ^{13}C NMR spectrum of ***o*-CO** in $CDCl_3$.

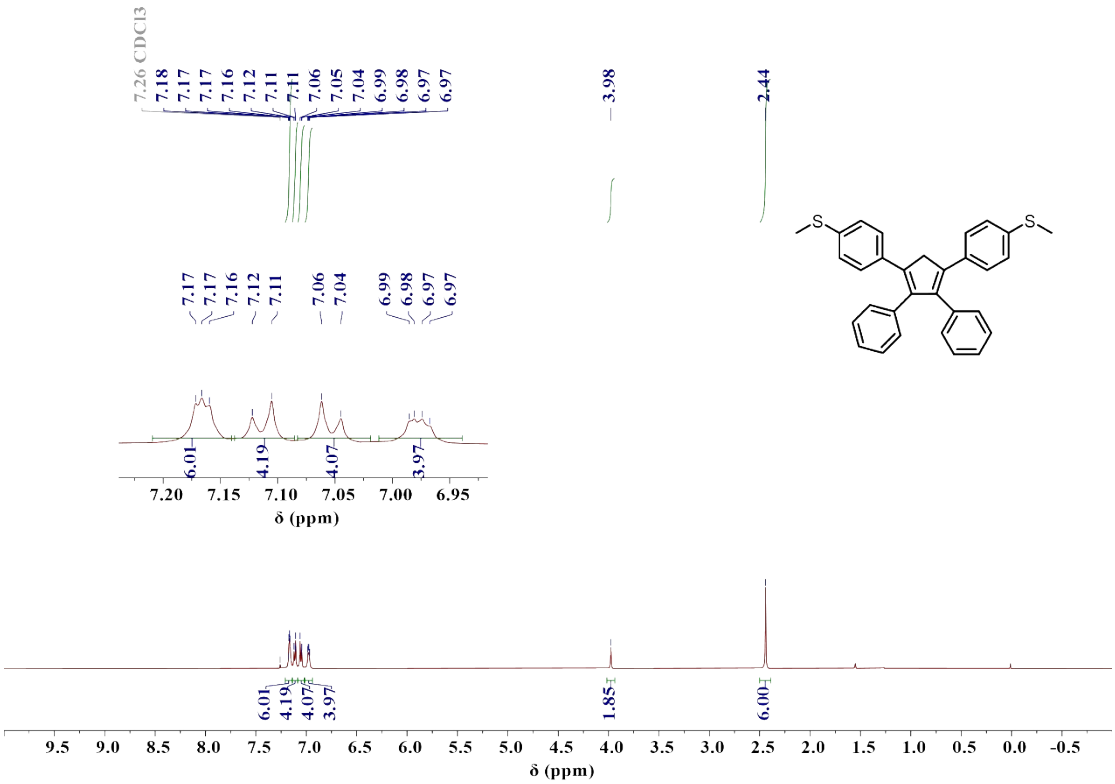

Fig. S7 ^{1}H NMR spectrum of ***m*-CH$_2$** in $CDCl_3$.

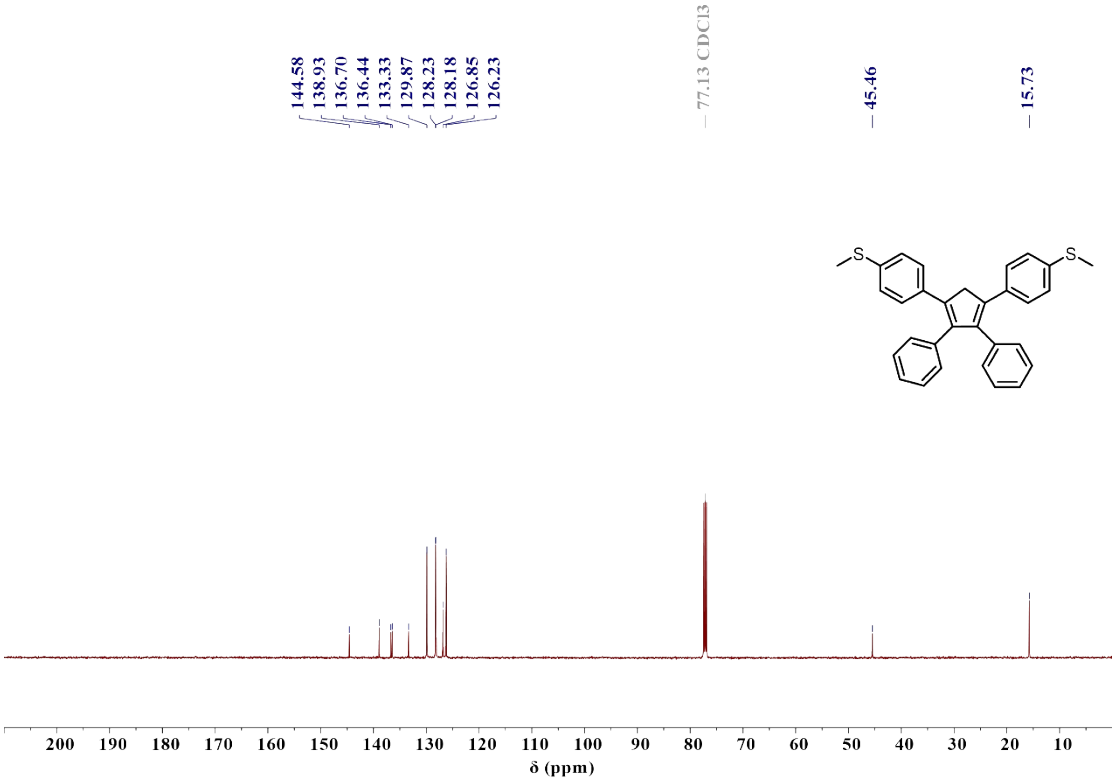

Fig. S8 ^{13}C NMR spectrum of ***m*-CH$_2$** in $CDCl_3$.

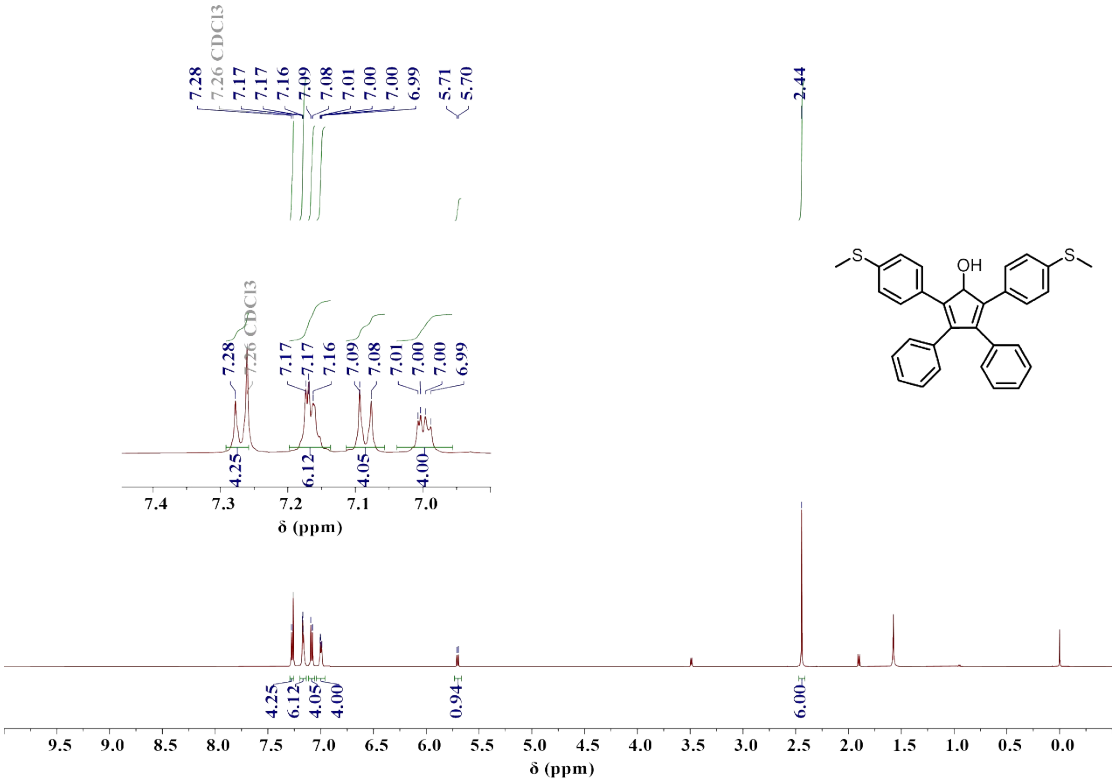

Fig. S9 ^{1}H NMR spectrum of ***m*-CHOH** in $CDCl_3$.

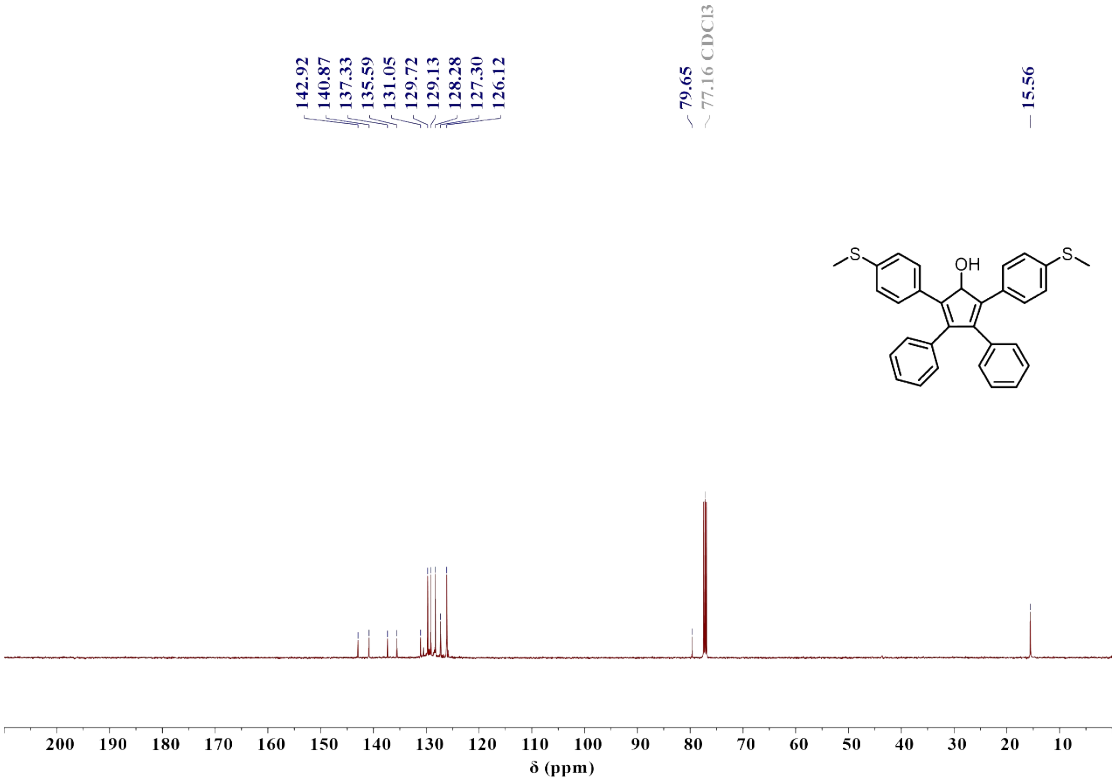

Fig. S10 ^{13}C NMR spectrum of ***m*-CHOH** in $CDCl_3$.

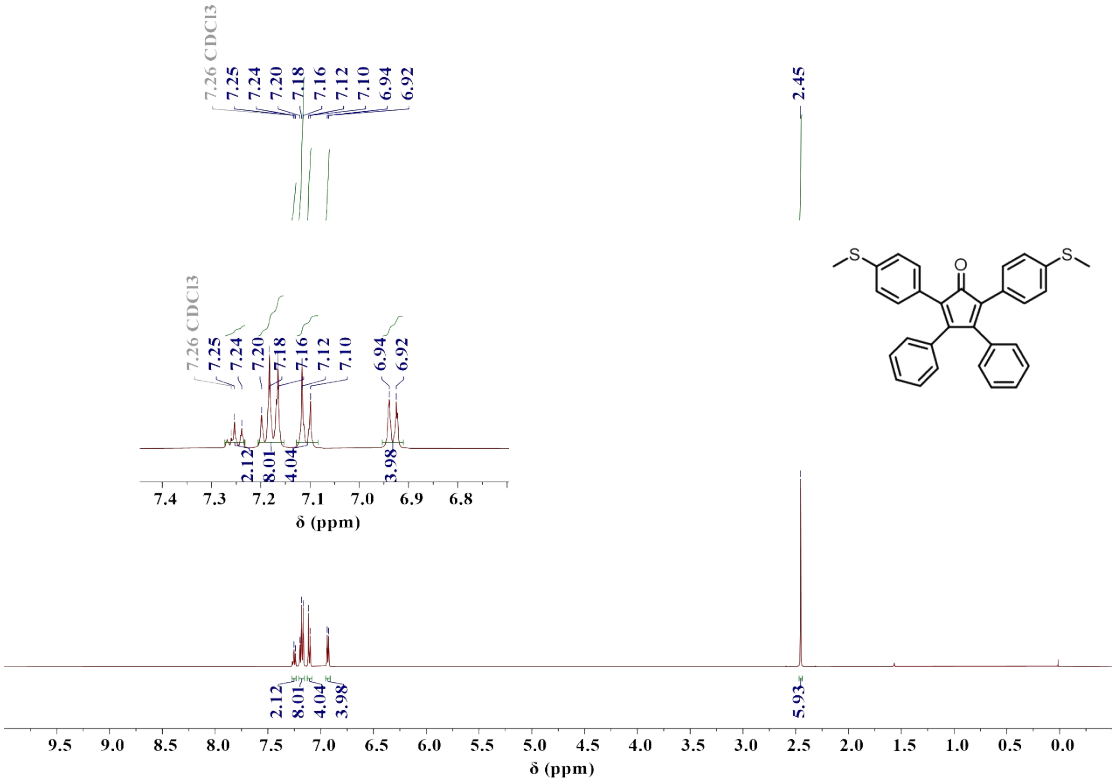

Fig. S11 ^{1}H NMR spectrum of ***m*-CO** in $CDCl_3$.

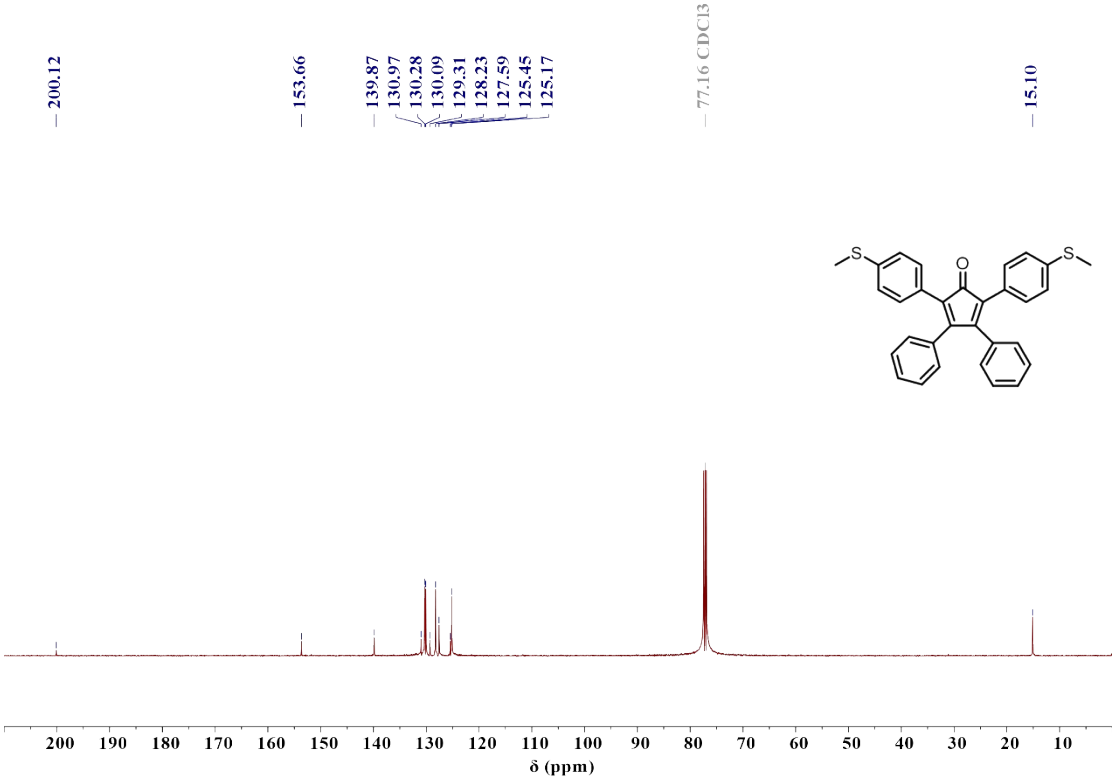

Fig. S12 ^{13}C NMR spectrum of ***m*-CO** in $CDCl_3$.

3. HRMS characterization

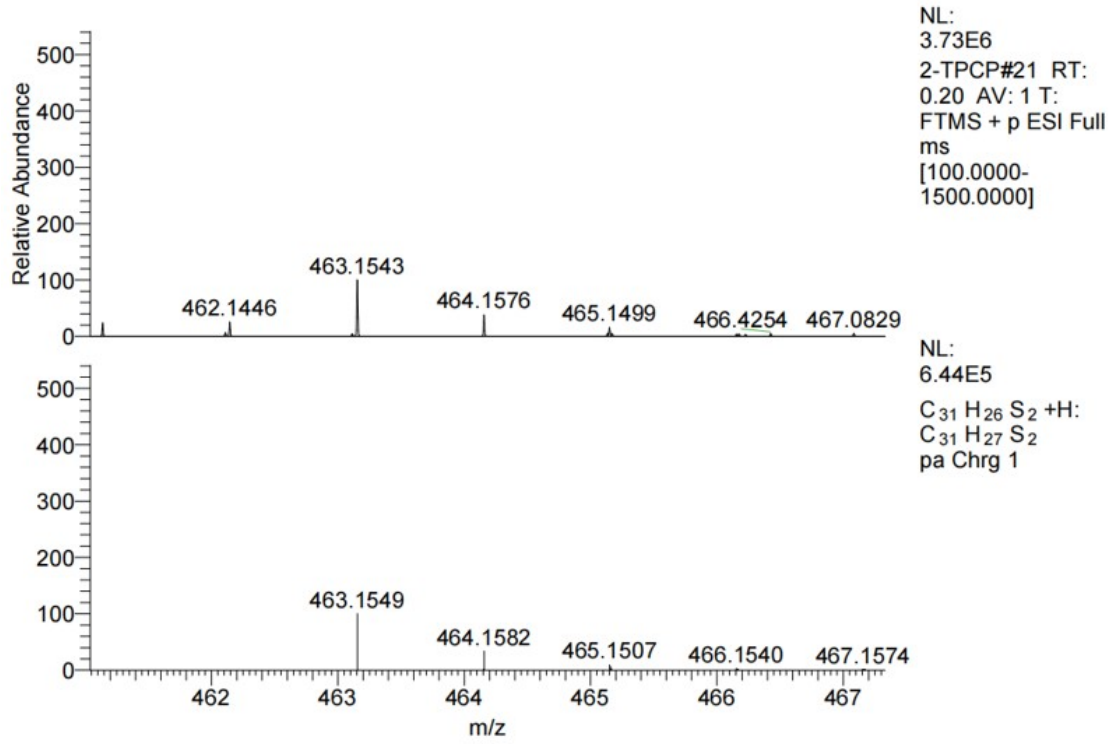

Fig. S13 HRMS of ***o*-CH_2**.

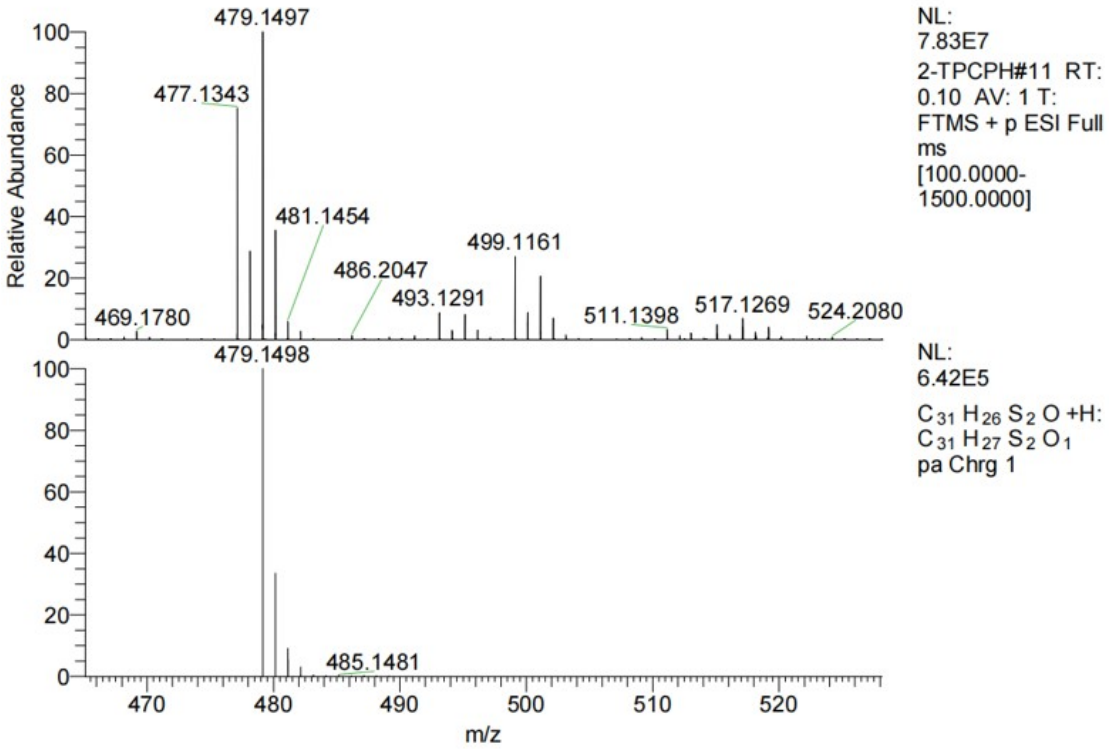

Fig. S14 HRMS of ***o*-CHOH**.

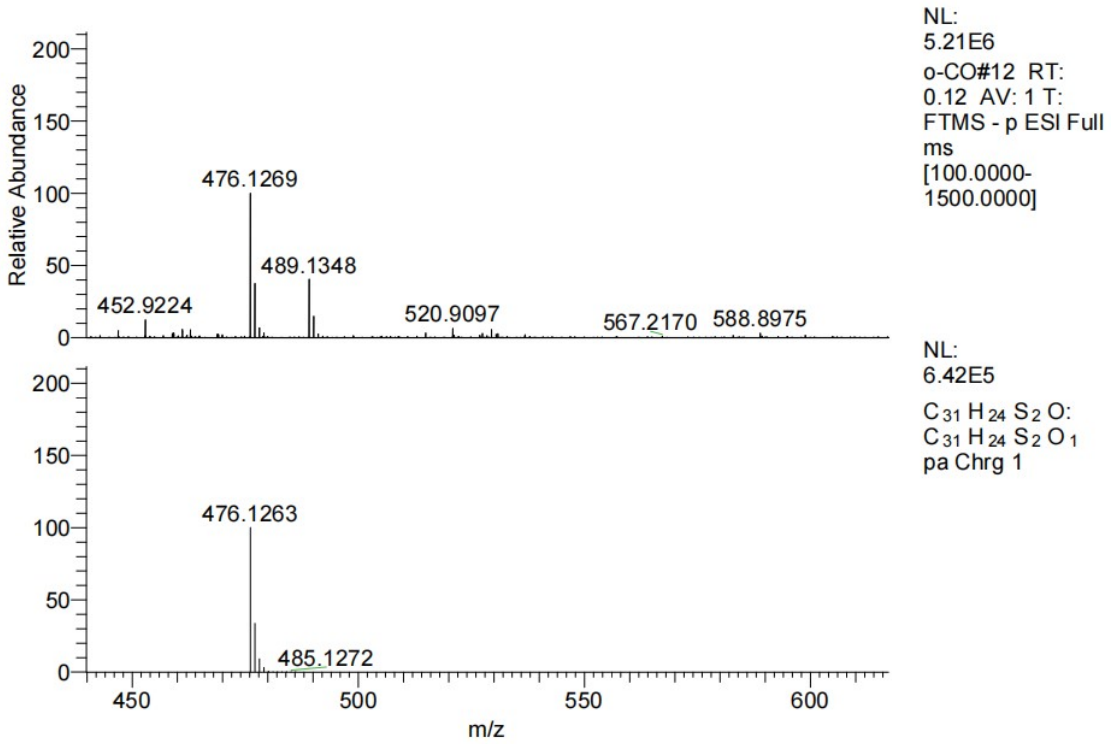

Fig. S15 HRMS of ***o*-CO**.

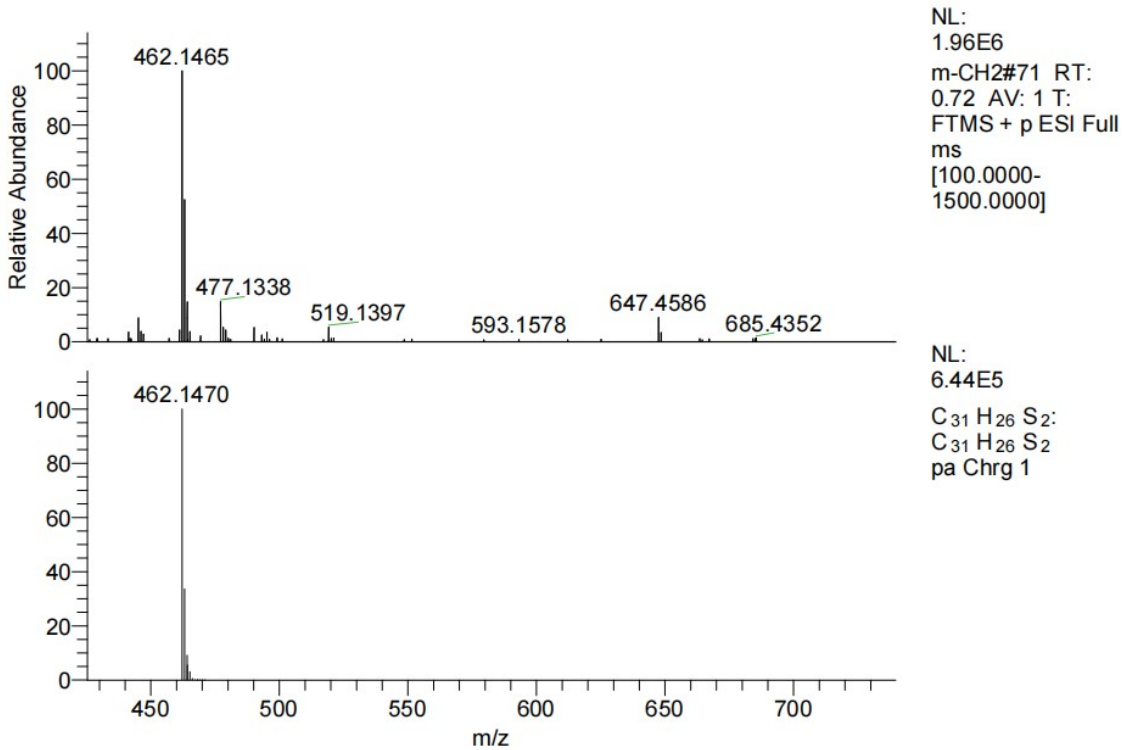

Fig. S16 HRMS of ***m*-CH_2**.

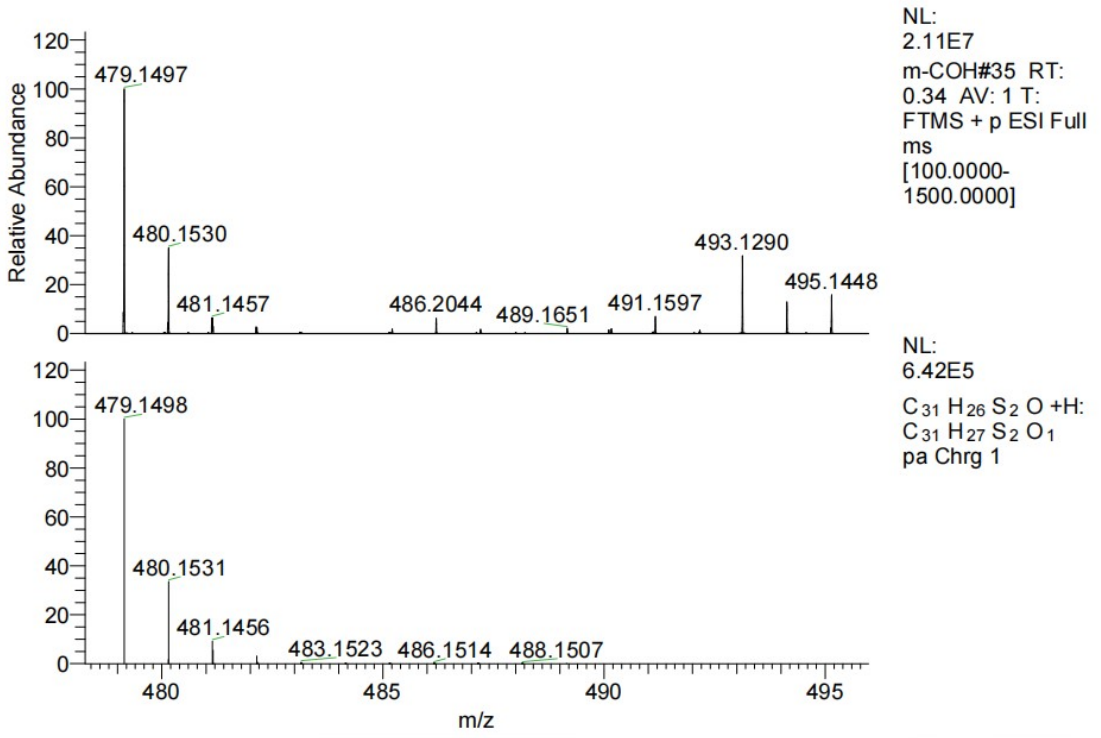

Fig. S17 HRMS of ***m*-CHOH**.

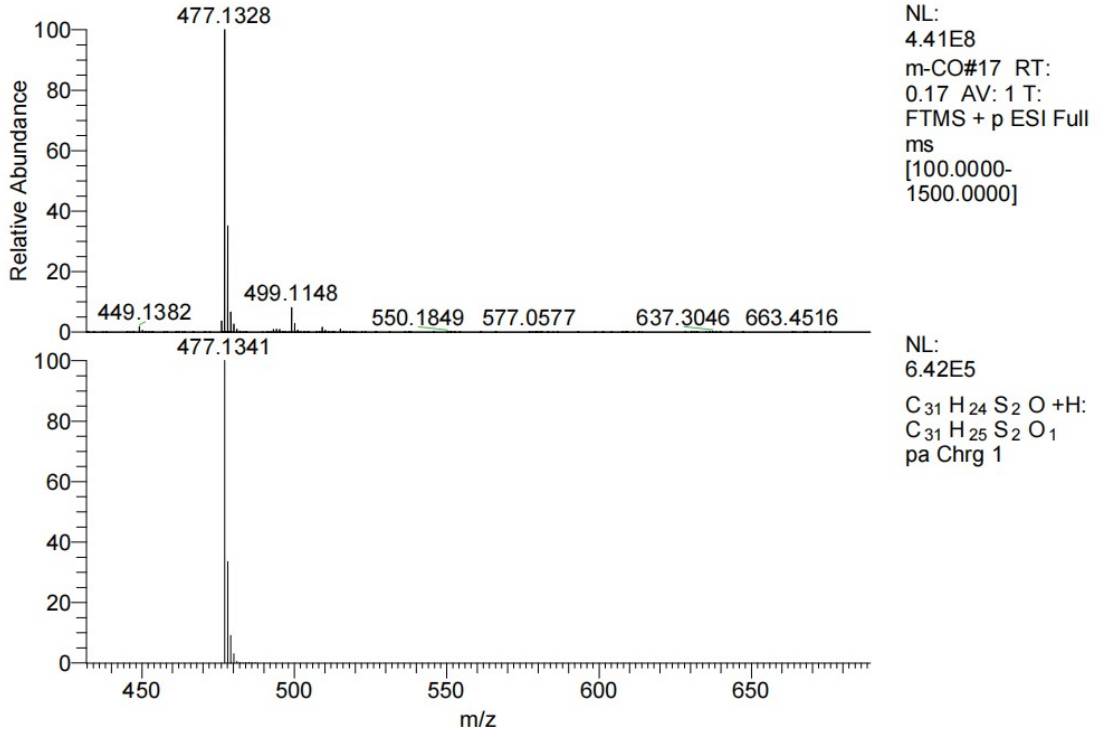

Fig. S18 HRMS of ***m*-CO**.

4. IR spectroscopy

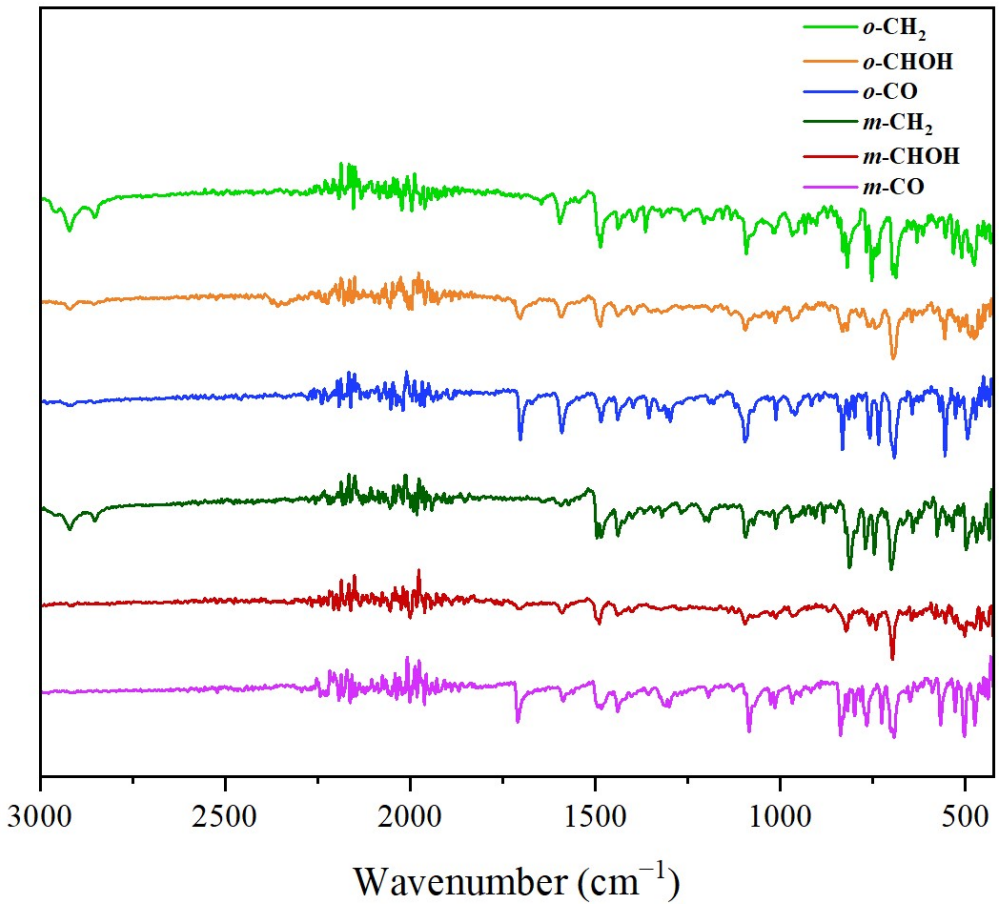

Fig. S19 Infrared spectra of cyclopentadienone derivatives.

Table S1. Significant IR absorption peaks for cyclopentadienone derivatives.

Compound	Wavenumber (cm^{-1})
***o*-CH_2**	686.0, 753.1, 819.1, 1092.0, 1485.4, 1595.8, 2852.7, 2920.2
***o*-CHOH**	694.7, 819.1, 1094.4, 1485.9
***o*-CO**	494.2, 554.4, 691.3, 831.7, 1095.4, 1590.5, 1701.9
***m*-CH_2**	699.5, 814.3, 1094.4, 1439.1, 1495.0, 2850.3, 2919.7
***m*-CHOH**	697.1, 822.5, 1096.8, 1489.3
***m*-CO**	502.6, 692.8, 836.5, 1085.2, 1709.1

5. Crystal data

Table S2. Crystallographic data and collection parameters for ***o*-CO** and ***m*-CO**.

Compound	***o*-CO**	***m*-CO**
CCDC number	2467116	2467115
Empirical formula	$C_{31}H_{24}OS_2$	$C_{31}H_{24}OS_2$
Formula weight	476.65	476.65
Temperature/K	296.15	296.15
Crystal system	monoclinic	monoclinic
Space group	$P2_1/n$	$I2/a$
a/Å	8.5837 (7)	8.5628 (3)
b/Å	22.8831 (13)	10.5389 (4)
c/Å	12.2993 (8)	27.4925 (8)
α/°	90	90
β/°	95.418 (7)	93.278 (3)
γ/°	90	90
Volume/Å^3	2405.10 (3)	2476.93 (15)
Z	4	4
μ/mm^{-1}	0.244	0.237
F (000)	1000.0	1000.0
2θ range/°	3.560 to 50.054	2.960 to 52.720
Reflections collected	40094	9649
Independent reflections	4234	2503
Data/restraints/parameters	4234/0/309	2503/0/156
Goodness-of-fit on F^2	1.034	1.042
Final R indices	R_1 = 0.0517 wR_2 = 0.1131	R_1= 0.0554 wR_2= 0.1155
R indices	R_1 = 0.0885 wR_2 = 0.1307	R_1 = 0.1003 wR_2 = 0.1402

6. UV-vis absorption spectroscopy and extinction coefficients

Table S3. Absorption maxima and extinction coefficients for UV-vis spectra of cyclopentadienone derivatives, λ_{max} reported in nm, and ε in M^{-1} cm^{-1}.

Compound	λ_1	ε_1	λ_2	ε_2	λ_3	ε_3
***o*-CH_2**	289	842	352	321	510	3
***o*-CHOH**	287	544	362	229	514	7
***o*-CO**	285	602	392	368	540	27
***m*-CH_2**	297	500	373	535	511	4
***m*-CHOH**	284	556	386	373	520	18
***m*-CO**	286	987	364	186	548	84

7. Theoretical calculations

7.1 Frontier molecular orbitals

Table S4. HOMO–LUMO energy levels of cyclopentadienone derivatives.

	***o*-CH_2**	***o*-CHOH**	***o*-CO**	***m*-CH_2**	***m*-CHOH**	***m*-CO**
HOMO (eV)	5.01	5.08	5.28	4.82	4.89	5.06
LUMO (eV)	1.35	1.56	2.66	1.35	1.57	2.68
Gap (eV)	3.67	3.52	2.62	3.47	3.32	2.39

7.2 Comparison of dihedral angles determined from XRD/DFT

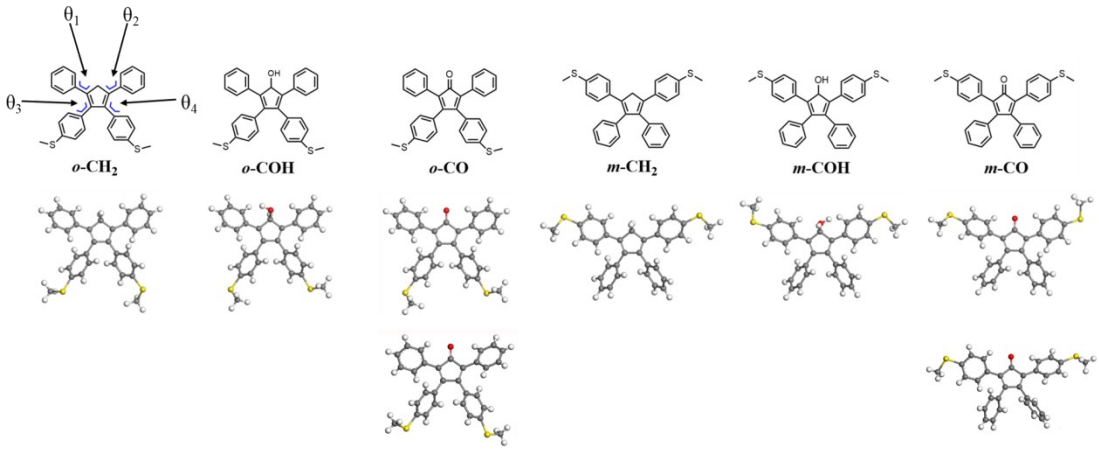

Fig. S20 Molecular structures of cyclopentadienone derivatives with dihedral-angle definitions. Dihedral angles θ1–θ4 are defined on ***o*-CH2** (left) and apply to all six derivatives, denoting, in order, the torsion between the phenyl substituents at the 2-, 5-, 3-, and 4-positions and the core five-membered ring. Top row: structural drawings with dihedral-angle labels. Middle row: geometry-optimized structures. Bottom row: room-temperature single-crystal structures (available for two derivatives).

Table S5. Comparison of XRD and DFT B3LYP-D3(BJ)/6-31G(d) dihedral angles for the rings of cyclopentadienone derivatives.

Compound	θ_1 (°)	θ_2 (°)	θ_3 (°)	θ_4 (°)
***o*-CH$_2$** (DFT)	31.72	31.69	57.22	57.25
***o*-CHOH** (DFT)	34.31	33.60	56.72	54.78
***o*-CO** (DFT)	37.96	37.35	52.59	52.41
***m*-CH$_2$** (DFT)	35.01	34.40	54.87	54.68
***m*-CHOH** (DFT)	34.65	39.99	52.40	54.17
***m*-CO** (DFT)	40.53	40.78	49.35	49.84
***o*-CO** (XRD)	33.36	36.40	55.72	43.96
***m*-CO** (XRD)	31.11	31.11	60.19	60.19

7.3 Transmission eigenstate and MPSH calculations

Table S6. MPSH orbital contributions to the transmission eigenstate of ***o*-CH_2** at E_F.

Orbital index (MPSH)	Projection weight
63	0.0045
80	0.0054
83	0.0019
107	0.0014
108	0.0029
112	0.0100
113	0.0014
114	0.0348
115	0.0772
116	0.0046
120	0.0049
121	0.0157
122	0.0131
123	0.0088
124	0.0010
126	0.1119
128	0.6837
138	0.0013
143	0.0017
144	0.0012
147	0.0013
150	0.0016

Table S7. MPSH orbital contributions to the transmission eigenstate of ***o*-CHOH** at E_F.

Orbital index (MPSH)	Projection weight
68	0.0022
72	0.0010
86	0.0026
93	0.0011
112	0.0019
117	0.0027
121	0.0967
122	0.0014
124	0.0060
125	0.0095
126	0.0020
127	0.0267
129	0.1554
131	0.6757
146	0.0022
150	0.0012
153	0.0013

Table S8. MPSH orbital contributions to the transmission eigenstate of ***o*-CO** at E_F.

Orbital index (MPSH)	Projection weight
64	0.0011
69	0.0012
114	0.0022
115	0.0059
116	0.0077
117	0.0123
129	0.1081
130	0.8399
141	0.0012
143	0.0052
147	0.0036
150	0.0014

Table S9. MPSH orbital contributions to the transmission eigenstate of ***m*-CH$_2$** at E_F

Orbital index (MPSH)	Projection weight
72	0.0015
74	0.0039
84	0.0012
85	0.0014
92	0.0015
98	0.0037
112	0.0031
113	0.0018
125	0.1436
126	0.6907
127	0.0304
128	0.0689
131	0.0012
134	0.0057
135	0.0027
136	0.0028
138	0.0060
139	0.0019
144	0.0050
145	0.0041
146	0.0015
147	0.0017
148	0.0020
200	0.0022

Table S10. MPSH orbital contributions to the transmission eigenstate of ***m*-CHOH** at E_F.

Orbital index (MPSH)	Projection weight
75	0.0041
95	0.0017
96	0.0025
97	0.0017
122	0.0021
123	0.0448
124	0.0347
125	0.0296
126	0.0126
128	0.0019
129	0.0706
130	0.1010
131	0.5535
132	0.1005
133	0.0222
146	0.0035
150	0.0010
156	0.0034

Table S11. MPSH orbital contributions to the transmission eigenstate of ***m*-CO** at E_F.

Orbital index (MPSH)	Projection weight
73	0.0012
89	0.0010
92	0.0048
93	0.0017
107	0.0012
115	0.0020
118	0.0046
120	0.0116
122	0.0178
123	0.0066
126	0.2303
127	0.0163
128	0.1863
129	0.0499
130	0.1991
131	0.2507
152	0.0021

7.4 Analysis of quantum interference effects

The influence of functional groups is relatively well understood, whereas the role of different transport pathways within molecules remains less clear. To address this, we employed a dual theoretical approach. For the complete cyclopentadienone derivatives, we applied extended curly arrow rules (ECAR) that are applicable to systems with interrupted conjugation to qualitatively assess their quantum interference effects.[1] Following this method, one anchoring unit is conceptually replaced with an electron donor (D) and the other with an electron acceptor (A). If a curly arrow pathway can be drawn to delocalize the D lone pair to A, constructive quantum interference (CQI) is predicted; otherwise, destructive quantum interference (DQI) is expected. Concurrently, to complement this analysis and decouple the pathway topology from complex substituent effects, we performed transport calculations on minimal model systems. The cyclopentadiene core, substituted with mercapto groups at either the 2,5- or 3,4-positions (corresponding to the *meta*- and *ortho*-anchoring patterns in the full series), was chosen for this purpose. Molecular junctions were constructed by adsorbing the Gaussian-optimized structures of 2,5- and 3,4-dimercapto-substituted cyclopentadiene onto a Au(111) vacancy, with the S–Au distance set to approximately 2.4 Å. Subsequently, transmission path analysis was performed on this molecular junction system to jointly support our argument (Fig. S21). For the specific analysis, the Quantum Atomistix ToolKit (Quantum ATK, version 2022.12) software package[2] was used, and the device adopted the generalized gradient approximation (GGA) Perdew-Burke-Ernzerhof (PBE) formulation as the exchange-correlation functional. The double-zeta plus polarization basis set was applied to all atoms except Au atoms, which had a double-zeta basis set. The grid cutoff energy was set to 100 Ry to save computation time.

We performed a transmission pathway analysis for the molecular junction both at the Fermi level and at energies near it, as shown in Fig. S21. For the 2,5-substituted (*meta*-series) pathway, although minor reversed pathways were present, the dominant transmission directions were consistent across three energies near the Fermi level,

indicating CQI. For the 3,4-substituted (*ortho*-series) pathway of cyclopentadiene, we observed quantum tunneling channels caused by the short distance, as well as multiple anti-resonant transmission channels in the opposite direction. These observations help explain the relatively small difference between DQI and CQI in the transmission spectra presented in the main text, as well as the shallow anti-resonance dip. These findings from the model system provide critical insight into the electronic behavior of the complete cyclopentadienone derivatives. Specifically, they suggest two plausible mechanisms to explain the relatively small difference between DQI and CQI and the shallow anti-resonance dip observed in the main text. First, the attenuation of the anti-resonance arises from the partial anti-resonances generated by the distinct transmission pathways. This results in incomplete DQI, which fails to fully suppress the transmission. It has been reported that in such cases, the anti-resonance occurs at complex energies, meaning that the transmission does not reach zero at real energies.[3–5] Second, the quantum tunneling observed in the core model implies that similar through-space transmission is likely active between the benzene rings at the 3- and 4-positions in the full derivative. This parallel conduction channel would elevate the transmission minimum, thereby contributing to the shallow anti-resonance dip.

The qualitative agreement between the ECAR results (Fig. S22) and the transmission pathway analysis (Fig. S21) indicates that the connection topology primarily determines the quantum interference nature, which in turn regulates the conductance trend across different isomeric series.

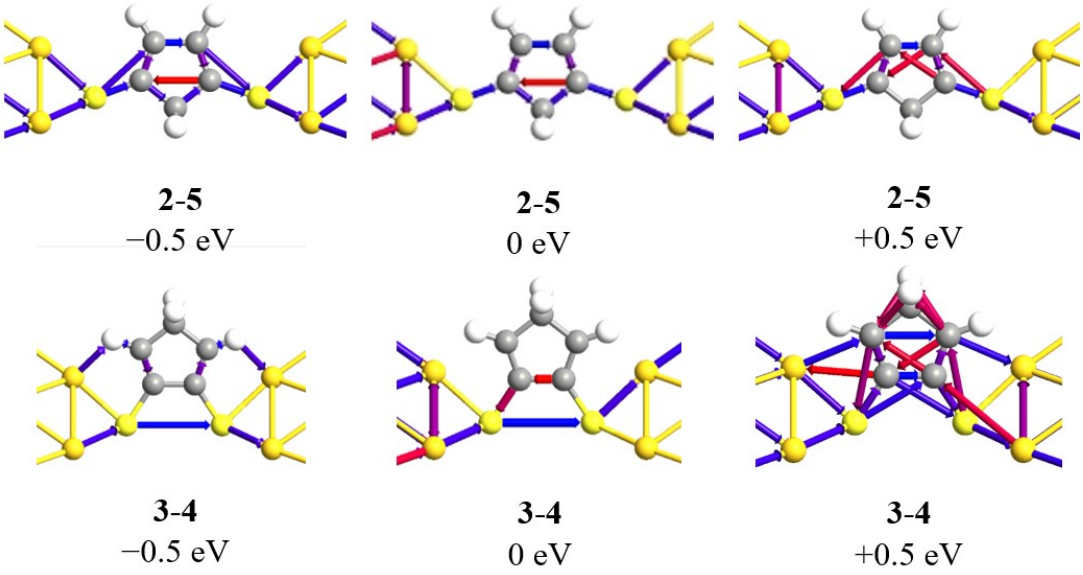

Fig. S21 Transmission pathway analysis at different energies for 2,5- and 3,4-dimercapto-substituted cyclopentadienes. The color of the arrows indicates the direction of transmission, and the size of the arrows is proportional to the transport contribution. The blue arrows represent positive channels, the red arrows represent negative channels, and the size of the transport contribution is indicated by the size of the arrows. For better comparison, the threshold of the paths is uniformly selected as 0.1.

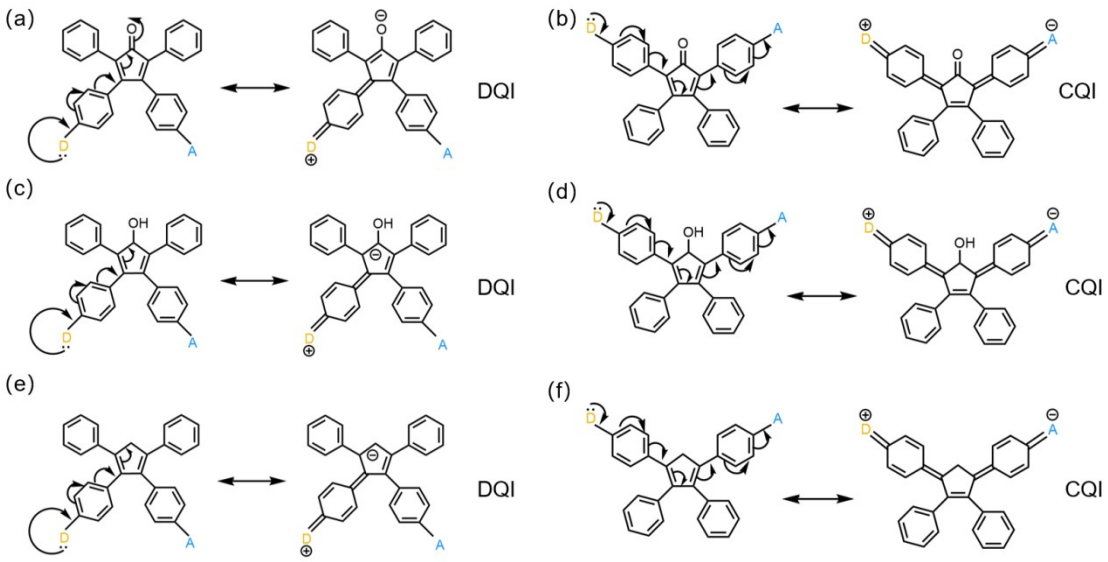

Fig. S22 Application of ECAR to the derivatives of cyclopentadienone

8. Break junction experiments

8.1 Blank solvent conductance test

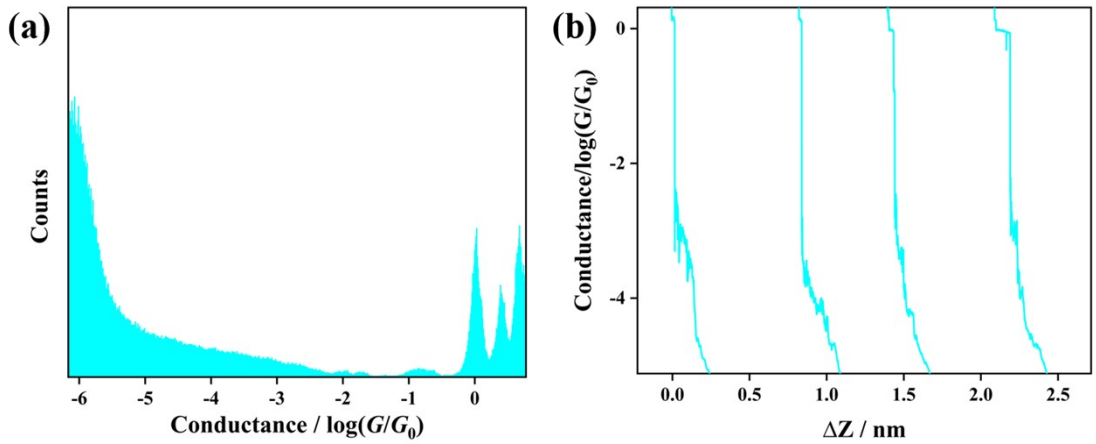

Fig. S23 (a) One-dimensional conductance histogram and molecular junction length distribution (inset) during pure solvent correction; (b) Single trace plot during pure solvent correction.

8.2 *I–V* Statistical Characterization

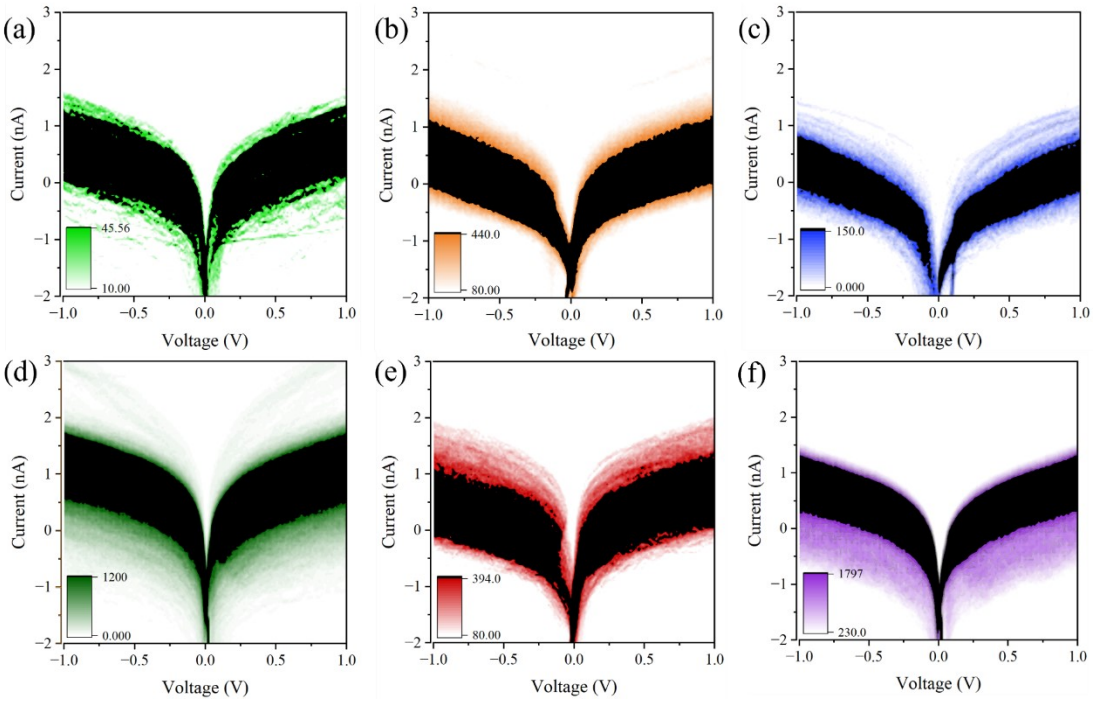

Fig. S24 2D histograms of the *nA–V* traces for each compound. The number of *I–V* traces in each is (a) ***o*-CH$_2$**, 7738; (b) ***o*-CHOH**, 11246; (c) ***o*-CO**, 8556; (d) ***m*-CH$_2$**, 9607; (e) ***m*-CHOH**, 12317; (f) ***m*-CO**, 9030.

Notes and references

1 L. J. O'Driscoll and M. R. Bryce, *Nanoscale*, 2021, **13**, 1103–1123.

2 S. Smidstrup, T. Markussen, P. Vancraeyveld, J. Wellendorff, J. Schneider, T. Gunst, B. Verstichel, D. Stradi, P. A. Khomyakov, U. G. Vej-Hansen, M.-E. Lee, S. T. Chill, F. Rasmussen, G. Penazzi, F. Corsetti, A. Ojanperä, K. Jensen, M. L. N. Palsgaard, U. Martinez, A. Blom, M. Brandbyge and K. Stokbro, *J. Phys.: Condens. Matter*, 2020, **32**, 015901.

3 P. Sam-ang and M. G. Reuter, *New J. Phys.*, 2017, **19**, 053002.

4 K. G. L. Pedersen, A. C. Borges, P. Hedegård, G. C. Solomon and M. Strange, *J. Phys. Chem. C*, 2015, **119**, 26919–26924.

5 M. H. Garner, H. Li, M. Neupane, Q. Zou, T. Liu, T. A. Su, Z. Shangguan, D. W. Paley, F. Ng, S. Xiao, C. Nuckolls, L. Venkataraman and G. C. Solomon, *J. Am. Chem. Soc.*, 2019, **141**, 15471–15476.